Numerical investigation of falling bacterial plumes caused by bioconvection in a three-dimensional chamber

Hyun Geun Lee [a], Junseok Kim [b,*]

[a] Institute of Mathematical Sciences, Ewha Womans University, Seoul 120-750, Republic of Korea
[b] Department of Mathematics, Korea University, Seoul 136-713, Republic of Korea

HIGHLIGHTS

- We investigate numerically the nonlinear dynamics of a 3D chemotaxis–fluid system without linearization and axisymmetry.
- We use an operator splitting-type Navier–Stokes solver to avoid a too strong restriction on the time step.
- We observe the formation of falling plumes and the convergence towards numerically stable stationary plumes.

ARTICLE INFO

ABSTRACT

Oxytactic bacteria like *Bacillus subtilis* are denser than water and swim up an oxygen gradient as they require certain minimum concentration of oxygen to be active. Due to upswimming, bacteria accumulate in a layer below the water surface and the density of an initially uniform suspension becomes greater near the water surface than the water bottom. When the upper bacteria-rich boundary layer is too dense, it becomes unstable and an overturning instability develops, leading to the formation of falling bacterial plumes. Bioconvection in modestly diluted cell suspensions is described by equations for concentrations of bacteria and oxygen together with the Navier–Stokes equations and the continuity equation. In this paper, we investigate numerically falling bacterial plumes caused by bioconvection in a three-dimensional chamber by solving the full chemotaxis–fluid coupled system. In numerical simulations of the system, the admissible time step is restricted by stability criteria due to a high Schmidt number, which corresponds to highly viscous fluids or low diffusion rates of bacteria. In order to avoid a too strong restriction on the time step, we use an operator splitting-type Navier–Stokes solver: the advection term is solved using a semi-Lagrangian method and the diffusion term is solved using the backward Euler method. We present numerical examples showing the formation of falling bacterial plumes out of random initial data and the convergence towards stationary bacterial plumes. And the merging of neighboring plumes is observed for a specific parameter set.

1. Introduction

In this paper, we consider the formation of falling plumes in a three-dimensional chamber that contains a suspension of oxytactic bacteria like *Bacillus subtilis* [1–3]. These bacteria are denser than water, consume oxygen, and swim up an oxygen gradient as they require certain minimum concentration of oxygen to be active. The upper surface of the chamber is open to the atmosphere and oxygen is replenished by diffusion from that surface. In a shallow chamber, the oxygen concentration throughout the chamber is high enough to allow all bacteria to swim actively. But, if the chamber is deep, the oxygen concentration below a certain depth is very low (since the diffusivity of oxygen in water is very small and bacteria consume oxygen) and, therefore, bacteria in the lower region of the chamber become inactive. Due to upswimming, bacteria accumulate in the upper layer of water and the density of an initially uniform suspension becomes greater at the top than the bottom. When the upper bacteria-rich boundary layer is too dense, it becomes unstable and an overturning instability develops, leading to the formation of falling bacterial plumes. The plumes transport bacteria and oxygen from the upper boundary layer, which is rich in bacteria and oxygen, to the lower region of the chamber, which is depleted of both bacteria and oxygen.

* Corresponding author. Tel.: +82 2 3290 3077; fax: +82 2 929 8562.
E-mail address: cfdkim@korea.ac.kr (J. Kim).
URL: http://math.korea.ac.kr/~cfdkim (J. Kim).
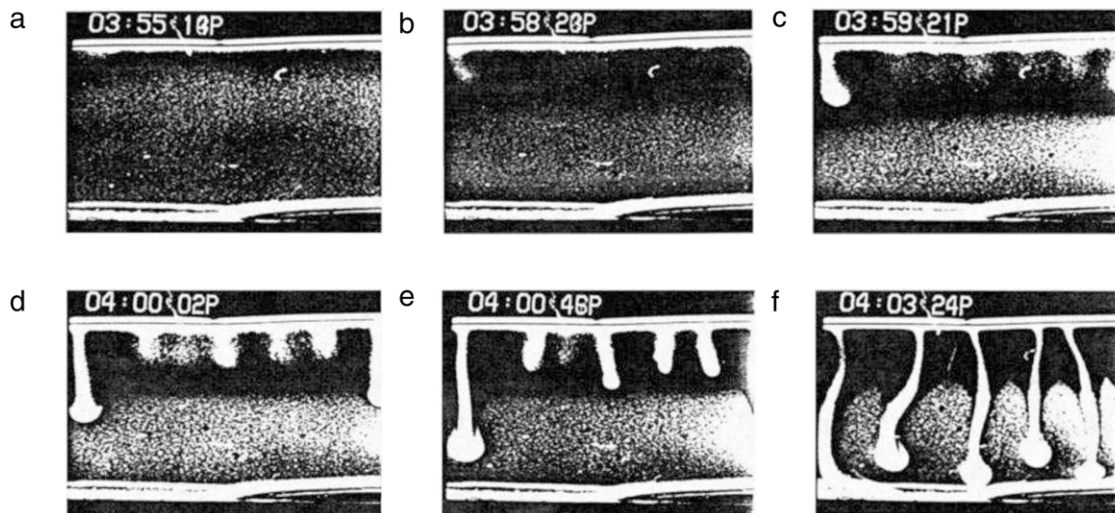
Fig. 1. Time sequence of photographs of a deep chamber containing a suspension of oxytactic bacteria like *Bacillus subtilis*. The successive times are shown at the upper left of each photograph.
Source: Photograph reproduced from Hillesdon et al. [1].

Fig. 1 shows time sequence of photographs of a deep chamber containing a suspension of bacteria reproduced from Hillesdon et al. [1]. The initial suspension is well mixed and quasi-homogeneous (Fig. 1(a)). First, a bacteria-rich upper boundary layer develops near the surface as bacteria swim up an oxygen gradient (Fig. 1(b)). Later, in Fig. 1(c)–(e), we can see the formation of falling bacterial plumes as the upper layer becomes unstable. The bacteria-rich plumes, which descend from the surface, carry oxygen from the surface and, in Fig. 1(f), some of the inactive bacteria in the lower region have been resuscitated by the oxygen carried by the descending plumes.

Bioconvection [4–7] in modestly diluted cell suspensions is described by equations for concentrations of bacteria and oxygen are coupled with the incompressible Navier–Stokes equations and the continuity equation. Hillesdon and Pedley [8] analyzed the linear stability for this chemotaxis–fluid coupled system and Metcalfe and Pedley [9] discussed the weakly nonlinear stability. Lorz [10] obtained a local existence result for the system and related systems. Duan et al. [11] proved global existence for the system with the simpler Stokes equations for weak potential or small initial oxygen concentration. Di Francesco et al. [12] investigated existence issues and asymptotic behavior of a model with nonlinear cell diffusion in the bacteria equation.

Harashima et al. [13] simulated gravitactic bioconvection in two dimensions and studied the evolution of bioconvection from an initially uniform state. Ghorai and Hill [14–16] investigated the structure and stability of two-dimensional gyrotactic plumes in tall, narrow chambers with either stress-free sidewalls or periodic sidewalls using a conservative finite-difference scheme. They also studied gyrotactic bioconvection in an axisymmetric chamber [17]. Chertock et al. [18] derived a high-resolution vorticity-based hybrid finite-volume finite-difference scheme to understand the interplay of gravity and chemotaxis in the formation of two-dimensional plumes. All the computations in [13–18] were based on continuum models. Hopkins and Fauci [19] simulated two-dimensional bioconvection using point particles rather than a continuum model and examined the general effects of a variety of different responses by the micro-organisms, including geotaxis, gyrotaxis, and chemotaxis.

Although there have been many numerical studies in two dimensions [13–19], bioconvection in three dimensions has not been well simulated due to computational difficulties, except the works of Ghorai and Hill [20] and of Karimi and Paul [21]. However,

they concerned with gyrotaxis only (not chemotaxis) and used a low Schmidt number (= 20), in which the Schmidt number is a dimensionless number defined as the ratio of viscosity and mass diffusivity. Note that a typical value of the Schmidt number for *Bacillus subtilis* in water is 500 [3,18].

Although it is relatively easy to solve the two-dimensional problem, bioconvection is intrinsically three-dimensional. In this paper, we therefore investigate a realistic three-dimensional bioconvection model. This work, for the first time to the authors' knowledge, considers the nonlinear dynamics of a three-dimensional chemotaxis–fluid system without linearization and axisymmetry. And, to avoid a too strong restriction on the admissible time step in numerical simulations of the system due to a high Schmidt number, we use an operator splitting-type Navier–Stokes solver: the advection term is solved using a semi-Lagrangian method and the diffusion term is solved using the backward Euler method.

The paper is organized as follows. In Section 2, we introduce the governing equations and perform the nondimensionalization of the governing equations. In Section 3, a numerical solution is given. We present numerical examples showing the formation of falling bacterial plumes out of random initial data and the convergence towards stationary bacterial plumes in Section 4. And the merging of neighboring plumes is observed for a specific parameter set. Finally, conclusions are drawn in Section 5.

2. Governing equations

Several related coupled chemotaxis–fluid model systems have been proposed and studied in [1–3,18] to describe bioconvection of a suspension of oxytactic bacteria in an incompressible fluid under the assumptions that the contribution of bacteria to the bacteria–fluid suspension is sufficiently small (since the density of the bacteria suspension is approximately equal to the density of the fluid) and that more detailed cell–cell interactions (such as hydrodynamic interaction) are neglected. The system, in which equations for concentrations of bacteria (n) and oxygen (c) are coupled with the incompressible Navier–Stokes equations (using the Boussinesq approximation) and the continuity equation, is as follows:

$$n_t + \mathbf{u} \cdot \nabla n = D_n \Delta n - \chi \nabla \cdot [nr(c)\nabla c], \tag{1}$$

$$c_t + \mathbf{u} \cdot \nabla c = D_c \Delta c - n\kappa r(c), \tag{2}$$

$$\rho(\mathbf{u}_t + \mathbf{u} \cdot \nabla \mathbf{u}) = -\nabla p + \eta \Delta \mathbf{u} + nV_b(\rho_b - \rho)\mathbf{g}, \quad (3)$$

$$\nabla \cdot \mathbf{u} = 0, \quad (4)$$

where $\Delta := \partial_x^2 + \partial_y^2 + \partial_z^2$ is the Laplacian, n and c are concentrations of bacteria and oxygen, respectively, $\mathbf{u} = (u, v, w)$ is the fluid velocity, and p is the fluid pressure. D_n and D_c are diffusion constants for bacteria and oxygen, respectively, χ is the chemotactic sensitivity (it may be interpreted as $\chi = av_0/c_{air}$, where a is a characteristic length, v_0 is the chemotactic velocity, and c_{air} is the oxygen concentration of the air above the fluid), κ is the oxygen consumption rate, and $r(c)$ is the dimensionless cut-off function. The function $r(c)$ is unity at large c and vanishes rapidly for c below the cut-off c^*, and is approximated by the step function $r(c) = \Theta(c - c^*)$ [3,18]. In the present work, to speed up the computation, we regularize $r(c)$ by

$$r(c) = \frac{1}{2}\left(1 + \frac{c - c^*}{\sqrt{(c - c^*)^2 + \epsilon^2}}\right),$$

where $\epsilon > 0$ is a constant close to zero. ρ is the fluid density, η is the fluid viscosity, V_b and ρ_b are the bacterial volume and density (bacteria are about 10% denser than water), respectively, $\mathbf{g} = (0, 0, -g)$ is the gravity, and g is the gravitational acceleration.

In order to match the experiment depicted in Fig. 1, we consider the following boundary conditions for Eqs. (1)–(4), which are to be integrated in the three-dimensional region bounded by the planes $x = 0, L_x, y = 0, L_y$, and $z = 0, L_z$: the boundary condition at $z = L_z$ describes the fluid–air surface, where there is no cell flux, the oxygen will be saturated with the air oxygen concentration c_{air}, and the surface is stress-free:

$$\chi n r(c)c_z - D_n n_z = 0, \quad c = c_{air}, \quad u_z = v_z = w = 0$$

at $z = L_z$.

At $z = 0$, the cell and oxygen fluxes and the fluid velocity are supposed zero:

$$n_z = c_z = 0, \quad u = v = w = 0 \quad \text{at } z = 0.$$

Finally, periodic boundary conditions at the four sides of the domain, $x = 0, L_x$ and $y = 0, L_y$, are imposed to avoid any impact of these boundaries.

2.1. Nondimensionalization of the governing equations

In order to restate the dimensional chemotaxis–fluid coupled system (1)–(4) in dimensionless form, we rescale the variables as follows:

$$\mathbf{x}' = \frac{\mathbf{x}}{L}, \quad t' = \frac{D_n}{L^2}t, \quad c' = \frac{c}{c_{air}}, \quad n' = \frac{n}{n_r},$$

$$\mathbf{u}' = \frac{L}{D_n}\mathbf{u}, \quad p' = \frac{L^2}{\eta D_n}p, \quad \mathbf{g}' = \frac{\mathbf{g}}{g},$$

where L is a characteristic length and n_r is the characteristic cell density. This scaling is chosen for consistency and comparison with previously published work [3,18]. After dropping the prime notation in the rescaled variables, we obtain the following system:

$$n_t + \nabla \cdot (n\mathbf{u}) = \Delta n - \alpha \nabla \cdot [nr(c)\nabla c], \quad (5)$$

$$c_t + \nabla \cdot (c\mathbf{u}) = \delta \Delta c - \beta r(c)n, \quad (6)$$

$$\mathbf{u}_t + \mathbf{u} \cdot \nabla \mathbf{u} = -Sc \nabla p + Sc \Delta \mathbf{u} + \gamma Sc\, n\mathbf{g}, \quad (7)$$

$$\nabla \cdot \mathbf{u} = 0, \quad (8)$$

where $\mathbf{g} = (0, 0, -1)$. The five dimensionless parameters $\alpha, \beta, \gamma, \delta$, and the Schmidt number Sc are

$$\alpha := \frac{\chi c_{air}}{D_n}, \quad \beta := \frac{\kappa n_r L^2}{c_{air} D_n}, \quad \gamma := \frac{V_b n_r g(\rho_b - \rho)L^3}{\eta D_n},$$

$$\delta := \frac{D_c}{D_n}, \quad Sc := \frac{\eta}{D_n \rho}.$$
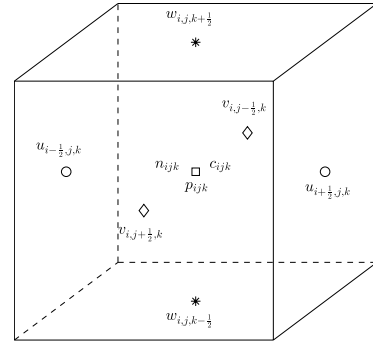
Fig. 2. Location of the variables on a MAC mesh cell.

The resulting system (5)–(8) is considered on a rectangular parallelepiped domain $\Omega = [0, l_x] \times [0, l_y] \times [0, l_z]$ subject to the initial data

$$n(x, y, z, 0) = n^0(x, y, z), \quad c(x, y, z, 0) = c^0(x, y, z),$$

$$\mathbf{u}(x, y, z, 0) = \mathbf{u}^0(x, y, z),$$

and the following boundary conditions: at the top and the bottom of Ω we set

$$\alpha nr(c)c_z - n_z = 0, \quad c = 1, \quad u_z = v_z = w = 0 \quad \text{at } z = l_z, \quad (9)$$

$$n_z = c_z = 0, \quad u = v = w = 0 \quad \text{at } z = 0, \quad (10)$$

while the periodic boundary conditions are applied at the four sides of Ω (that is, at $x = 0, l_x$ and $y = 0, l_y$).

3. Numerical solution

Let a three-dimensional computational domain be uniformly partitioned with spacing h. The cell center is located at $(x_i, y_j, z_k) = ((i - 0.5)h, (j - 0.5)h, (k - 0.5)h)$ for $i = 1, \ldots, N_x, j = 1, \ldots, N_y$, and $k = 1, \ldots, N_z$. N_x, N_y, and N_z are the numbers of cells in the x-, y-, and z-directions, respectively. Cell vertices are located at $(x_{i+\frac{1}{2}}, y_{j+\frac{1}{2}}, z_{k+\frac{1}{2}}) = (ih, jh, kh)$. Pressures and concentrations of bacteria and oxygen are stored at cell centers, and velocities are stored at cell faces [22] (Fig. 2).

In order to model a suspension of swimming bacteria *Bacillus subtilis* in water, we set the Schmidt number to $Sc = 500$ [3,18]. A high Schmidt number corresponds to highly viscous fluids or low diffusion rates of bacteria. For highly viscous fluids, an explicit treatment of the diffusion term $\Delta \mathbf{u}$ in Eq. (7) is subject to a severe restriction on the time step Δt. In order to use a much larger time step than an explicit method, we employ the "stable fluids" method of Stam [23]. Given the solution $\mathbf{u}(\mathbf{x}, t^m)$ where $\mathbf{x} = (x, y, z)$ and m is a time step index, the solution at $t^{m+1} = t^m + \Delta t$ is solved in four steps. The steps are: let $\mathbf{w}_0(\mathbf{x}) = \mathbf{u}(\mathbf{x}, t^m)$,

$$\mathbf{w}_0(\mathbf{x}) \overset{\text{add force}}{\longrightarrow} \mathbf{w}_1(\mathbf{x}) \overset{\text{advect}}{\longrightarrow} \mathbf{w}_2(\mathbf{x}) \overset{\text{diffuse}}{\longrightarrow} \mathbf{w}_3(\mathbf{x}) \overset{\text{project}}{\longrightarrow} \mathbf{w}_4(\mathbf{x}).$$

The solution $\mathbf{u}(\mathbf{x}, t^{m+1})$ is then given by the last velocity field: $\mathbf{u}(\mathbf{x}, t^{m+1}) = \mathbf{w}_4(\mathbf{x})$. The first step is to simply add the external force $\gamma Sc\, n\mathbf{g}$: $\mathbf{w}_1(\mathbf{x}) = \mathbf{w}_0(\mathbf{x}) + \Delta t (\gamma Sc\, n(\mathbf{x}, t^m)\mathbf{g})$. The second step accounts for the effect of advection of the fluid on itself. A disturbance in the velocity field propagates according to the advection term $-\mathbf{u} \cdot \nabla \mathbf{u}$. In order to obtain the new velocity $\mathbf{w}_2$ at a point $\mathbf{x}$, we backtrace the point $\mathbf{x}$ through the velocity field $\mathbf{w}_1$ over a time Δt. This defines a path $\mathbf{p}(\mathbf{x}, t)$ corresponding to a partial streamline of the velocity field. The new velocity $\mathbf{w}_2$ at the point $\mathbf{x}$ is then set to $\mathbf{w}_2(\mathbf{x}) = \mathbf{w}_1(\mathbf{p}(\mathbf{x}, -\Delta t))$. The third step solves for the effect of viscosity and uses an implicit method:

$$\mathbf{w}_3(\mathbf{x}) - Sc \Delta t \Delta \mathbf{w}_3(\mathbf{x}) = \mathbf{w}_2(\mathbf{x}). \quad (11)$$

(a) $u - z$.

(b) $x - w$.
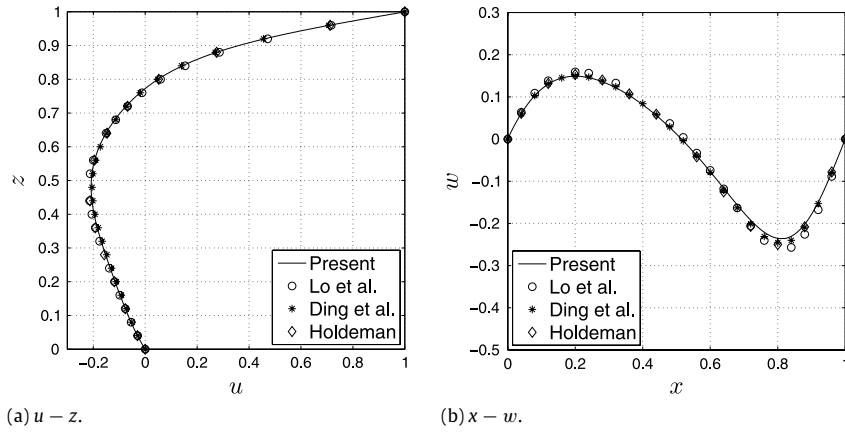
Fig. 3. Comparison of velocity component distribution along the (a) vertical and (b) horizontal centerlines of the plane $y = 0.5$ for 3D lid-driven cavity with $Re = 100$.
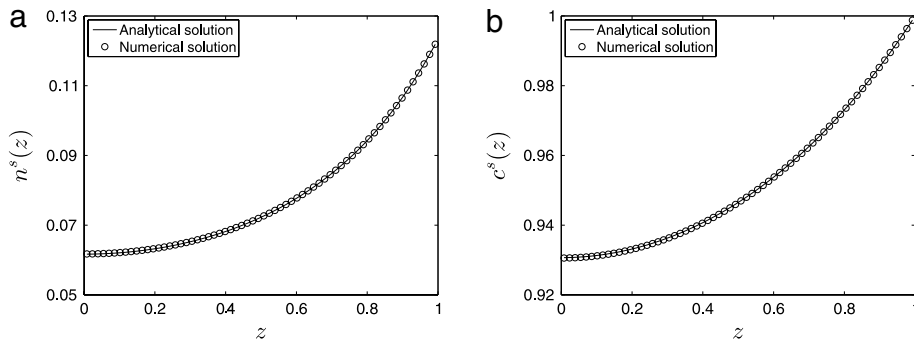
Fig. 4. Comparison of the numerical steady-state solutions (a) n and (b) c with the analytical steady-state solutions.

Finally, the last step projects the velocity field onto the divergence free field [24]. This step involves the solution of a Poisson equation

$$\Delta q = \frac{1}{Sc \Delta t} \nabla \cdot \mathbf{w}_3, \tag{12}$$

followed by the correction $\mathbf{w}_4 = \mathbf{w}_3 - Sc \Delta t \nabla q$. In Eqs. (11) and (12), the diffusion operator Δ can be discretized and the resulting sparse linear system can be solved by a fast solver, such as a linear multigrid method [25]. Also, a Gauss–Seidel relaxation scheme is used as the smoother in the multigrid method.

The quantities n and c are evolved in time by solving the chemotaxis equations (5) and (6) using a semi-implicit method:

$$\frac{n_{ijk}^{m+1} - n_{ijk}^m}{\Delta t} + \nabla_h \cdot (n\mathbf{u})_{ijk}^m = \Delta_h n_{ijk}^{m+1} - \alpha \nabla_h \cdot [nr(c)\nabla_h c]_{ijk}^m,$$

$$\frac{c_{ijk}^{m+1} - c_{ijk}^m}{\Delta t} + \nabla_h \cdot (c\mathbf{u})_{ijk}^m = \delta \Delta_h c_{ijk}^{m+1} - \beta [r(c)n]_{ijk}^m,$$

where

$$\nabla_h \cdot (\phi\mathbf{u})_{ijk}^m = \frac{u_{i+\frac{1}{2},j,k}^m(\phi_{i+1,j,k}^m + \phi_{ijk}^m) - u_{i-\frac{1}{2},j,k}^m(\phi_{ijk}^m + \phi_{i-1,j,k}^m)}{2h}$$

$$+ \frac{v_{i,j+\frac{1}{2},k}^m(\phi_{i,j+1,k}^m + \phi_{ijk}^m) - v_{i,j-\frac{1}{2},k}^m(\phi_{ijk}^m + \phi_{i,j-1,k}^m)}{2h}$$

$$+ \frac{w_{i,j,k+\frac{1}{2}}^m(\phi_{i,j,k+1}^m + \phi_{ijk}^m) - w_{i,j,k-\frac{1}{2}}^m(\phi_{ijk}^m + \phi_{i,j,k-1}^m)}{2h},$$

$$\Delta_h \phi_{ijk}^{m+1}$$

$$= \frac{\phi_{i+1,j,k}^{m+1} + \phi_{i,j+1,k}^{m+1} + \phi_{i,j,k+1}^{m+1} - 6\phi_{ijk}^{m+1} + \phi_{i-1,j,k}^{m+1} + \phi_{i,j-1,k}^{m+1} + \phi_{i,j,k-1}^{m+1}}{h^2}$$

for $\phi = n, \ c$ and

$$\nabla_h \cdot [nr(c)\nabla_h c]_{ijk}^m$$

$$= \frac{n_{i+\frac{1}{2},j,k}^m r\left(c_{i+\frac{1}{2},j,k}^m\right)(c_{i+1,j,k}^m - c_{ijk}^m) - n_{i-\frac{1}{2},j,k}^m r\left(c_{i-\frac{1}{2},j,k}^m\right)(c_{ijk}^m - c_{i-1,j,k}^m)}{h^2}$$

$$+ \frac{n_{i,j+\frac{1}{2},k}^m r\left(c_{i,j+\frac{1}{2},k}^m\right)(c_{i,j+1,k}^m - c_{ijk}^m) - n_{i,j-\frac{1}{2},k}^m r\left(c_{i,j-\frac{1}{2},k}^m\right)(c_{ijk}^m - c_{i,j-1,k}^m)}{h^2}$$

$$+ \frac{n_{i,j,k+\frac{1}{2}}^m r\left(c_{i,j,k+\frac{1}{2}}^m\right)(c_{i,j,k+1}^m - c_{ijk}^m) - n_{i,j,k-\frac{1}{2}}^m r\left(c_{i,j,k-\frac{1}{2}}^m\right)(c_{ijk}^m - c_{i,j,k-1}^m)}{h^2},$$

where $n_{i+\frac{1}{2},j,k}^m = (n_{i+1,j,k}^m + n_{ijk}^m)/2$ and the other terms are similarly defined.

4. Numerical examples

4.1. Validation of the Navier–Stokes solver: the lid-driven cavity flow

In order to examine the performance of the Navier–Stokes solver, described in the previous section, in the three-dimensional computation of highly viscous fluids, we consider the standard lid-driven cavity flow problem [26–30] for the following equations:

$$\mathbf{u}_t + \mathbf{u} \cdot \nabla \mathbf{u} = -\nabla p + \frac{1}{Re}\Delta \mathbf{u},$$

$$\nabla \cdot \mathbf{u} = 0,$$

where Re is the Reynolds number. The problem domain is a unit cube with the top lid moving parallel to the x-axis. The velocity $\mathbf{u}$ is set to zero on all faces except the upper face where the tangential component u is set to 1. We use $h = 1/64$, $\Delta t = 10h^2$, and
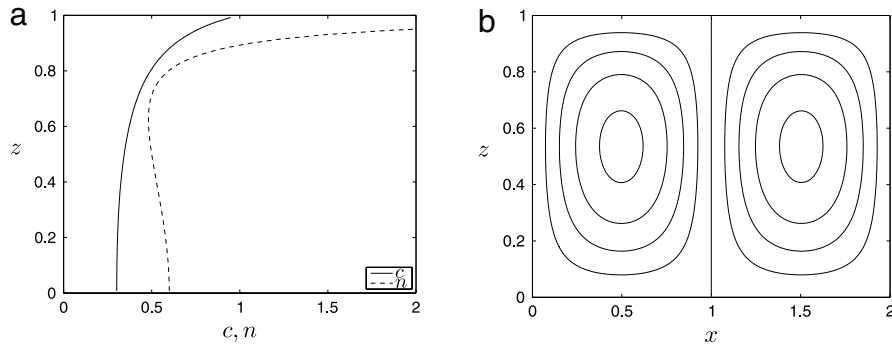
Fig. 5. (a) Vertical profiles of the oxygen c and cell n densities and (b) streamlines at $t = 0.22$ for $\alpha = 5$, $\beta = 5$, $\delta = 0.25$, $\gamma = 418$, and $Sc = 7700$.
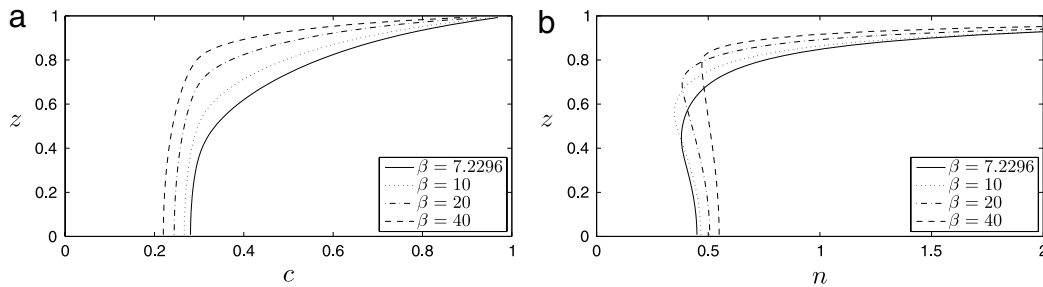
Fig. 6. Vertical profiles of (a) oxygen c and (b) cell n densities at $t = 0.22$ for $\alpha = 5$, $\delta = 1$, $\gamma = 418$, $Sc = 7700$, and $\beta = 7.2296, 10, 20, 40$.
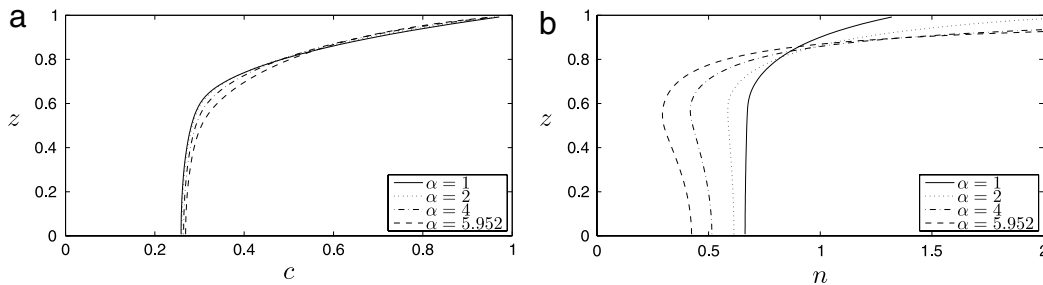
Fig. 7. Vertical profiles of (a) oxygen c and (b) cell n densities at $t = 0.22$ for $\beta = 10$, $\delta = 1$, $\gamma = 418$, $Sc = 7700$, and $\alpha = 1, 2, 4, 5.952$.

$Re = 100$. For the convergence criterion of steady flow, maximum norm of velocity difference between the new and old time levels, i.e. $\|\mathbf{u}^{m+1} - \mathbf{u}^m\|_\infty$, is set to be less than $5 \cdot 10^{-7}$.

For the purpose of validation, the u velocity profile along the vertical centerline ($u - z$ plot) and w velocity profile along the horizontal centerline ($x - w$ plot) of the plane $y = 0.5$ are computed. Since there is no available analytical expression for the solution, the numerical solutions of previous literature are adopted as references to validate the present results. Fig. 3(a) and (b) show the $u - z$ and $x - w$ comparisons with the results of Lo et al. [28], Ding et al. [29], and Holdeman [30], respectively. It can be seen that the velocity profiles agree well with those of the above authors.

4.2. Comparison of numerical and analytical steady-state solutions

It is known from Hillesdon et al. [1] that for suitable parameters solutions of (5)–(8) converge to homogeneous-in-x, y steady-state solutions of the following system:

$$\Delta n = \alpha \nabla \cdot [nr(c)\nabla c], \qquad \delta \Delta c = \beta r(c)n. \tag{13}$$

The analytical solutions $n^s(z)$ and $c^s(z)$ of (13) can be explicitly computed provided that $c \geq c^*$ and, thus, $r(c) = 1$ in the entire domain [1], and are given by

$$n^s(z) = \frac{\delta A^2}{\beta} \frac{\alpha}{2} \sec^2\left(\frac{\alpha}{2}Az\right),$$

$$c^s(z) = 1 - \frac{2}{\alpha} \ln\left(\frac{\cos\left(\frac{\alpha}{2}Az\right)}{\cos\left(\frac{\alpha}{2}A\right)}\right),$$

where A is a constant and determined from the following transcendental equation:

$$\tan\left(\frac{\alpha}{2}A\right) = \frac{\beta}{\delta A} \int_0^1 n^s(z)\,dz.$$

We now solve numerically the system (5)–(8) with $\alpha = 10$, $\beta = 10$, $\gamma = 1000$, $\delta = 5$, and $Sc = 500$. The initial conditions are

$$n^0(x, y, z) = \frac{\pi}{40}, \qquad c^0(x, y, z) = 1, \qquad \mathbf{u}^0(x, y, z) = \mathbf{0}$$

on the domain $\Omega = [0, 2] \times [0, 2] \times [0, 1]$. We take the cut-off $c^* = 0.3$, $A = \pi/20$, $h = 1/64$, $\Delta t = 4 \cdot 10^{-5}$, and $\epsilon = h$. We run the code until the numerical solution converges to its steady state. Fig. 4(a) and (b) show the vertical profiles of the numerical steady-state solutions n and c, respectively. It can be seen that the numerical and analytical solutions are in good agreement.

4.3. Comparison with previous results

Hillesdon and Pedley [8] investigated how the parameter values δ, β_{HP}, and γ_{HP} affect the results (note that there is a difference in
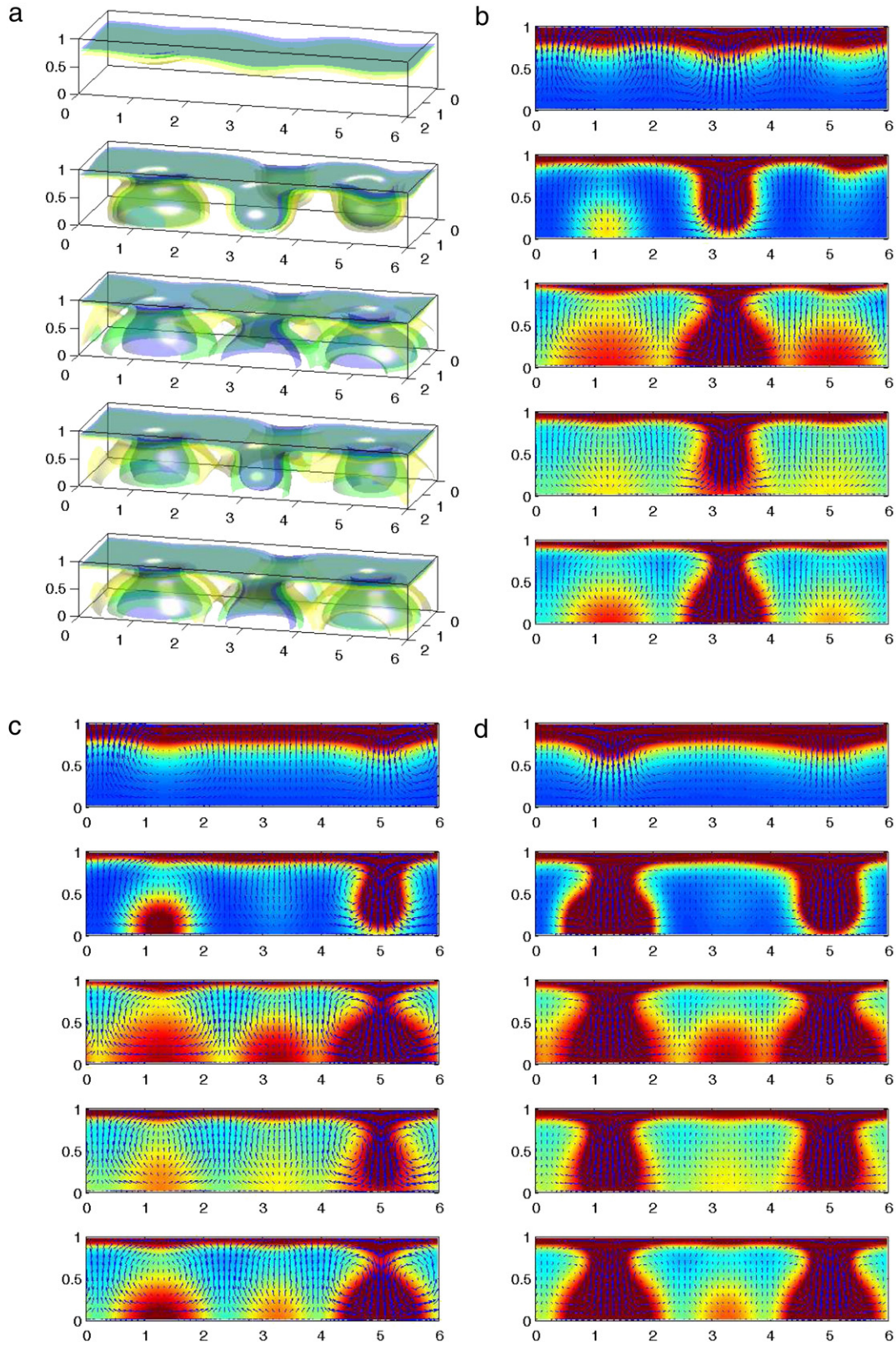
Fig. 8. (a) Cell density $n(x, y, z, t)$ and (b)–(d) bioconvection patterns in the x–z cross section at $y = 0, 0.5$, and 1 at different times $t = 0.32, 0.37, 0.42, 0.47$, and 0.52 (from top to bottom). In (a), yellow, green, and blue isosurfaces correspond to $n(x, y, z, t) = 0.5, 0.75$, and 1, respectively. In (b)–(d), color contours represent the cell concentration $n(x, y, z, t)$ with red representing large concentrations and blue representing small concentrations, and arrows represent the velocity components $u(x, y, z, t)$ and $w(x, y, z, t)$ at $y = 0, 0.5$, and 1. (For interpretation of the references to color in this figure legend, the reader is referred to the web version of this article.)

the definition of parameters compared to [8], i.e., $\alpha \rightarrow \gamma_{HP}$, $\beta/\delta \rightarrow \beta_{HP}$, and $\gamma \rightarrow \Gamma_{HP}$). We here consider an example presented in [8]

for $\gamma = 418$ and $Sc = 7700$. We take the cut-off $c^* = 0.3$ and the following initial conditions:
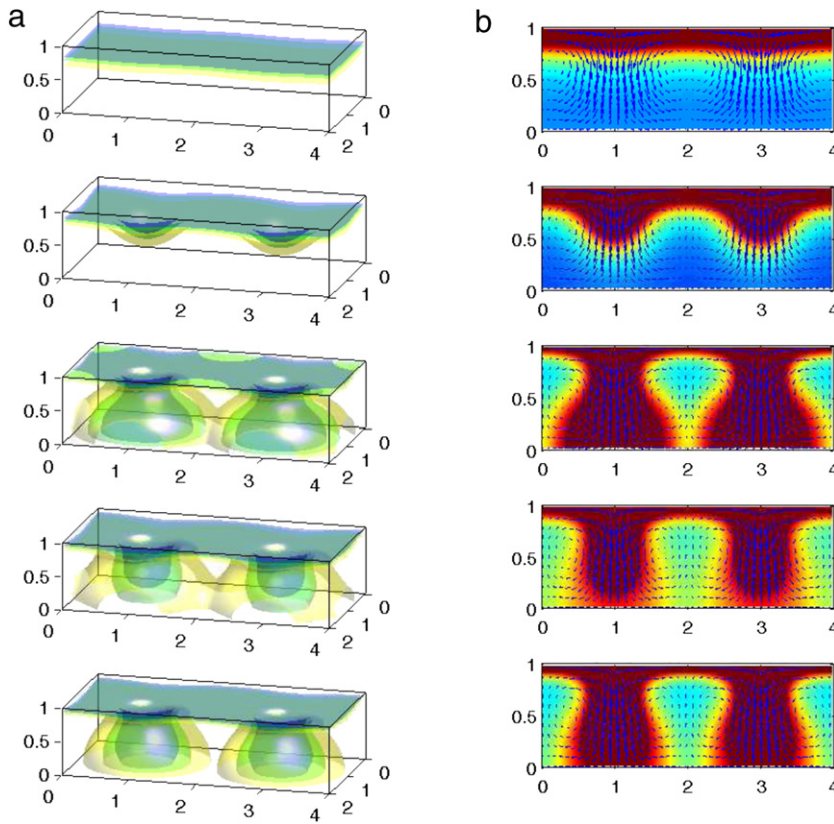
Fig. 9. (a) Cell density $n(x, y, z, t)$ and (b) bioconvection pattern in the x–z cross section at $y = 1$ at different times $t = 0.2, 0.27, 0.34, 0.39$, and 0.78 (from top to bottom). In (a), yellow, green, and blue isosurfaces correspond to $n(x, y, z, t) = 0.5, 0.75$, and 1, respectively. In (b), color contours represent the cell concentration $n(x, 1, z, t)$ with red representing large concentrations and blue representing small concentrations, and arrows represent the velocity components $u(x, 1, z, t)$ and $w(x, 1, z, t)$. (For interpretation of the references to color in this figure legend, the reader is referred to the web version of this article.)
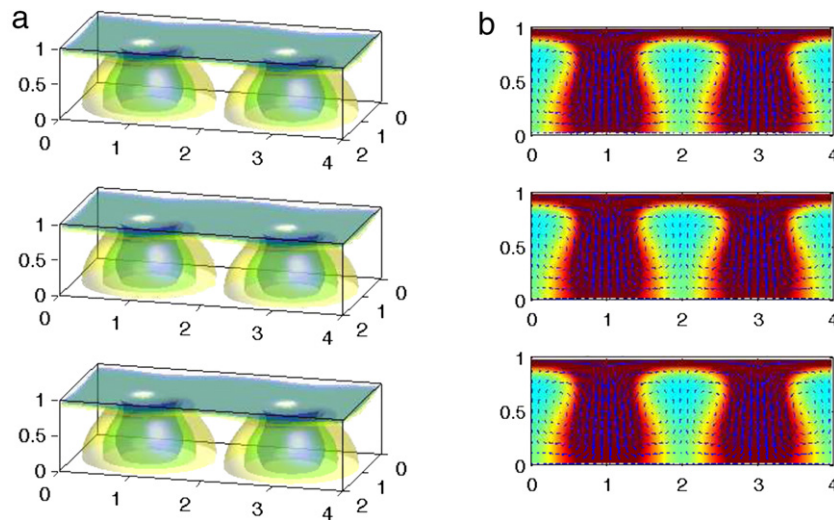
Fig. 10. Effect of δ. For $\delta = 5$, (a) cell density $n(x, y, z, t)$ and (b) bioconvection pattern in the x–z cross section at $y = 1$ at different times $t = 3.9, 4.4$, and 4.9 (from top to bottom). In (a), yellow, green, and blue isosurfaces correspond to $n(x, y, z, t) = 0.5, 0.75$, and 1, respectively. In (b), color contours represent the cell concentration $n(x, 1, z, t)$ with red representing large concentrations and blue representing small concentrations, and arrows represent the velocity components $u(x, 1, z, t)$ and $w(x, 1, z, t)$. (For interpretation of the references to color in this figure legend, the reader is referred to the web version of this article.)

$$n^0(x, y, z) = \begin{cases} 1 & \text{if } z > 0.501 - 0.01(\sin((x - 0.5)\pi) \\ & + \sin((y - 0.5)\pi)), \\ 0.5 & \text{otherwise}, \end{cases}$$

$$c^0(x, y, z) = 1, \qquad \mathbf{u}^0(x, y, z) = \mathbf{0}$$

on the domain $\Omega = [0, 2] \times [0, 2] \times [0, 1]$, which prescribes small sinusoidal modulations of the lower edge of the upper layer with

cell concentration higher than at the bottom. The grid spacing and time step used in our calculations are $h = 1/64$ and $\Delta t = 4 \cdot 10^{-5}$, respectively, and we use $\epsilon = h$.

Fig. 5(a) shows the vertical profiles of the computed quasi-homogeneous-in-x, y oxygen c and cell n densities at $t = 0.22$ for $\alpha = 5$, $\beta = 5$, and $\delta = 0.25$. These are in qualitative agreement with the Figure 14 in [8]. Note that the vertical profile of the cell
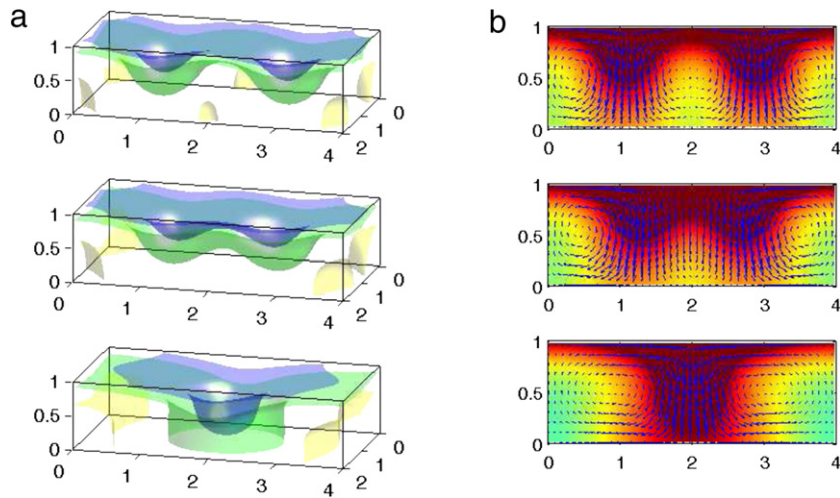
Fig. 11. Effect of δ. For $\delta = 25$, (a) cell density $n(x, y, z, t)$ and (b) bioconvection pattern in the x–z cross section at $y = 1$ at different times $t = 2.9, 3.4$, and 3.9 (from top to bottom). In (a), yellow, green, and blue isosurfaces correspond to $n(x, y, z, t) = 0.5, 0.75$, and 1, respectively. In (b), color contours represent the cell concentration $n(x, 1, z, t)$ with red representing large concentrations and blue representing small concentrations, and arrows represent the velocity components $u(x, 1, z, t)$ and $w(x, 1, z, t)$. (For interpretation of the references to color in this figure legend, the reader is referred to the web version of this article.)
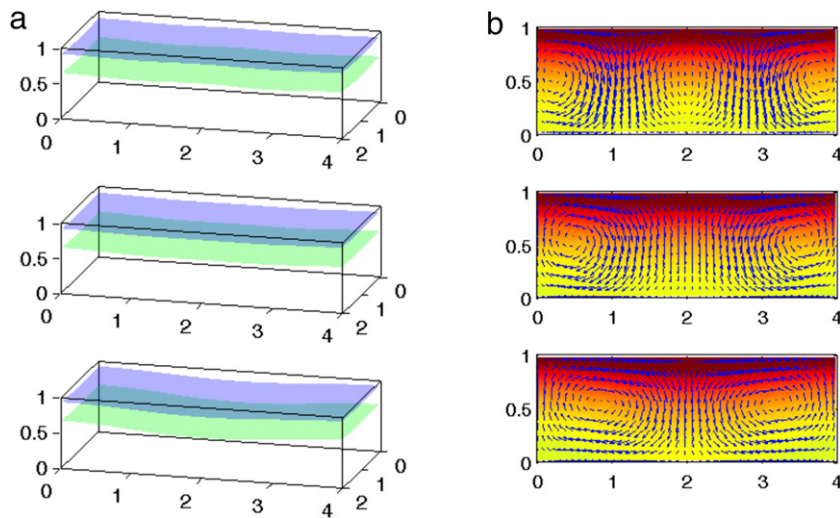
Fig. 12. Effect of δ. For $\delta = 50$, (a) cell density $n(x, y, z, t)$ and (b) bioconvection pattern in the x–z cross section at $y = 1$ at different times $t = 1.9, 2.4$, and 2.9 (from top to bottom). In (a), yellow, green, and blue isosurfaces correspond to $n(x, y, z, t) = 0.5, 0.75$, and 1, respectively. In (b), color contours represent the cell concentration $n(x, 1, z, t)$ with red representing large concentrations and blue representing small concentrations, and arrows represent the velocity components $u(x, 1, z, t)$ and $w(x, 1, z, t)$. (For interpretation of the references to color in this figure legend, the reader is referred to the web version of this article.)

density shows an increase of cells towards the bottom, which is due to the cut-off of the chemotactic convection for oxygen levels below $c \leq c^*$. And the bioconvection pattern is well captured by the streamlines shown in Fig. 5(b).

Next, we vary the value of β for $\alpha = 5$ and $\delta = 1$. The vertical profiles of the oxygen c and cell n densities at $t = 0.22$ for $\beta = 7.2296, 10, 20, 40$ are shown in Fig. 6. The increase in the value of β (α and δ fixed) indicates that the oxygen consumption increases relative to the oxygen diffusion. Thus, as the value of β increases, the oxygen density at the same vertical position decreases (Fig. 6(a)) and the cell upswimming increases (Fig. 6(b)). These are in qualitative agreement with the Figure 9 in [8].

We also vary the value of α for $\beta = 10$ and $\delta = 1$. The vertical profiles of the oxygen c and cell n densities at $t = 0.22$ for $\alpha = 1, 2, 4, 5.952$ are shown in Fig. 7. The increase in the value of α (β and δ fixed) indicates that the directed cell swimming increases relative to the diffusive swimming. Thus, as the value of α increases, the cell density near the surface increases, the cells vacate the lower regions of the chamber more rapidly (Fig. 7(b)), and less overall

oxygen consumption occurs in these regions (Fig. 7(a)). These are in qualitative agreement with the Figure 12 in [8].

4.4. Bacterial bioconvection in three dimensions

In the following subsections, we describe numerical experiments with the system (5)–(8) on the rectangular parallelepiped domain subject to various initial conditions and the boundary conditions (9) and (10). In these examples, we set the coefficients $\alpha = 10, \beta = 10, \gamma = 1000, \delta = 5$, and the Schmidt number $Sc = 500$ to model a suspension of swimming bacteria *Bacillus subtilis* in water [3,18], and take the cut-off $c^* = 0.3$. The grid spacing and time step used in our calculations are $h = 1/32$ and $\Delta t = 10^{-4}$, respectively, and we use $\epsilon = h$.

4.4.1. Time evolution of randomly perturbed homogeneous initial data

We here consider homogeneous initial data with a random perturbation in the cell concentration:
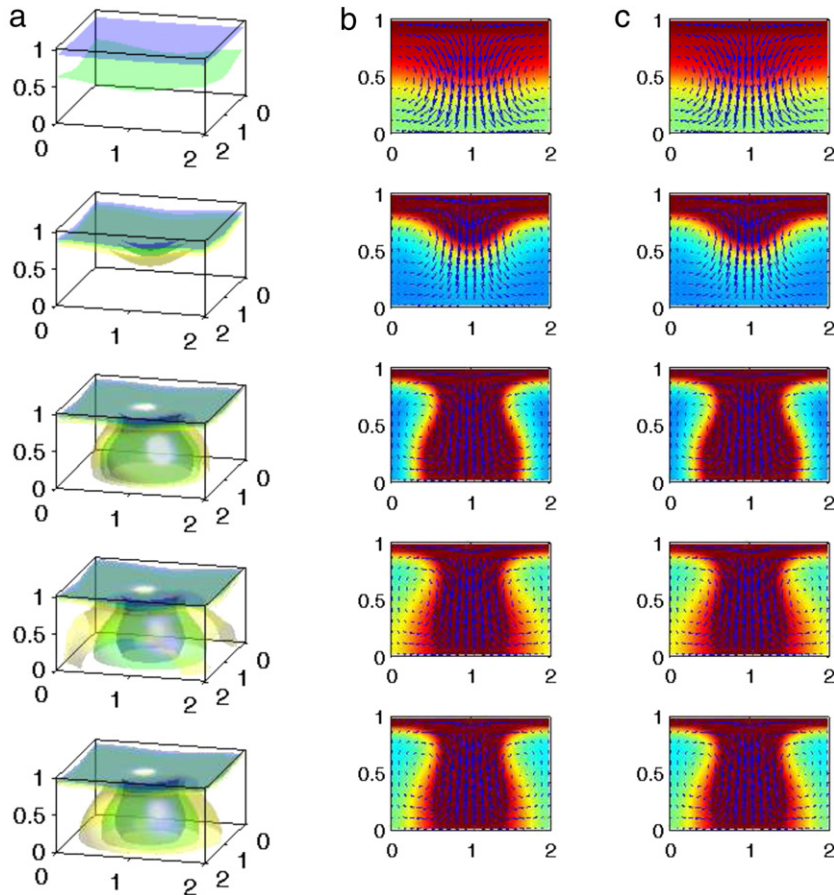
Fig. 13. For $n_{3D}^0(x, y, z)$, (a) cell density $n(x, y, z, t)$ and (b)–(c) bioconvection patterns in the x–z cross section at $y = 1$ and the y–z cross section at $x = 1$ at different times $t = 0.01, 0.2, 0.24, 0.29,$ and 0.59 (from top to bottom). In (a), yellow, green, and blue isosurfaces correspond to $n(x, y, z, t) = 0.5, 0.75,$ and 1, respectively. In (b) (or (c)), color contours represent the cell concentration $n(x, 1, z, t)$ (or $n(1, y, z, t)$) with red representing large concentrations and blue representing small concentrations, and arrows represent the velocity components $u(x, 1, z, t)$ and $w(x, 1, z, t)$ (or $v(1, y, z, t)$ and $w(1, y, z, t)$). (For interpretation of the references to color in this figure legend, the reader is referred to the web version of this article.)

$$n^0(x, y, z) = 0.8 + 0.2\text{rand}(\,), \qquad c^0(x, y, z) = 1,$$

$$\mathbf{u}^0(x, y, z) = \mathbf{0},$$

where rand( ) is a random number uniformly distributed in the interval [0, 1]. The computational domain is $\Omega = [0, 6] \times [0, 2] \times [0, 1]$.

Fig. 8(a) shows the time evolution of the cell density n. The concentration $n(x, y, z, t)$ at different times is plotted as isosurfaces, and yellow, green, and blue isosurfaces correspond to $n(x, y, z, t) = 0.5, 0.75,$ and 1, respectively. The cell concentration at the top (bottom) of the chamber increases (decreases) with time due to cells swimming upwards and accumulating at the top, and thus we observe several instabilities at a high-concentration layer below the fluid–air surface at $t = 0.32$. These instabilities developed into three falling plumes at $t = 0.37$ and all plumes hit the bottom of the chamber at $t = 0.42$. The cells in the bottom of the plumes move into the periphery of the plumes, swim, and are advected by the fluid towards the fluid–air surface, and thus we observe smaller plumes and thicker cell-rich layer at $t = 0.47$ than those at $t = 0.42$. After $t = 0.52$, the patterns seem to be stationary are observed. Fig. 8(b)–(d) show the bioconvection patterns in the x–z cross section at $y = 0, 0.5,$ and 1, respectively, for each of the rows of Fig. 8(a). Color contours represent the cell concentration $n(x, y, z, t)$ at $y = 0, 0.5,$ and 1 with red representing large concentrations and blue representing small concentrations. Arrows represent the velocity components $u(x, y, z, t)$ and $w(x, y, z, t)$ at $y = 0, 0.5,$ and 1. Fig. 8(b)–(d) illustrate that in regions of large concentrations the fluid velocity is downward, as indicated by the falling plumes.

4.4.2. Time evolution of deterministic initial data

In this section, we study the time evolution of solutions of (5)–(8) from the following purely deterministic initial data:

$$n^0(x, y, z) = \begin{cases} 1 & \text{if } z > 0.499 - 0.01(\sin((x - 0.5)\pi) \\ & \quad + \sin((y - 0.5)\pi)), \\ 0.5 & \text{otherwise,} \end{cases}$$

$$c^0(x, y, z) = 1, \qquad \mathbf{u}^0(x, y, z) = \mathbf{0}$$

on the domain $\Omega = [0, 4] \times [0, 2] \times [0, 1]$.

Fig. 9(a) and (b) show cell density $n(x, y, z, t)$ and bioconvection pattern in the x–z cross section at $y = 1$ at different times, respectively. At around $t = 0.2$, the solution starts developing instabilities, and at $t = 0.27$, two plumes are emerging according to the small perturbations in the initial cell concentration. These plumes hit the bottom of the chamber at $t = 0.34$ and slightly bounce upwards at $t = 0.39$. From $t = 0.39$ to $t = 0.78$, there is only a small change in the shape or size of the plumes. After $t = 0.78$, the plumes become steady.

4.4.3. Effect of increased δ

In order to investigate how a variation in the parameter δ affects the time evolution of the cell density, we perform tests with the following initial data:

$$n^0(x, y, z) = \begin{cases} 1 & \text{if } z > 0.499 - 0.05(\sin((x - 0.5)\pi) \\ & \quad + \sin((y - 0.5)\pi)), \\ 0.5 & \text{otherwise,} \end{cases}$$
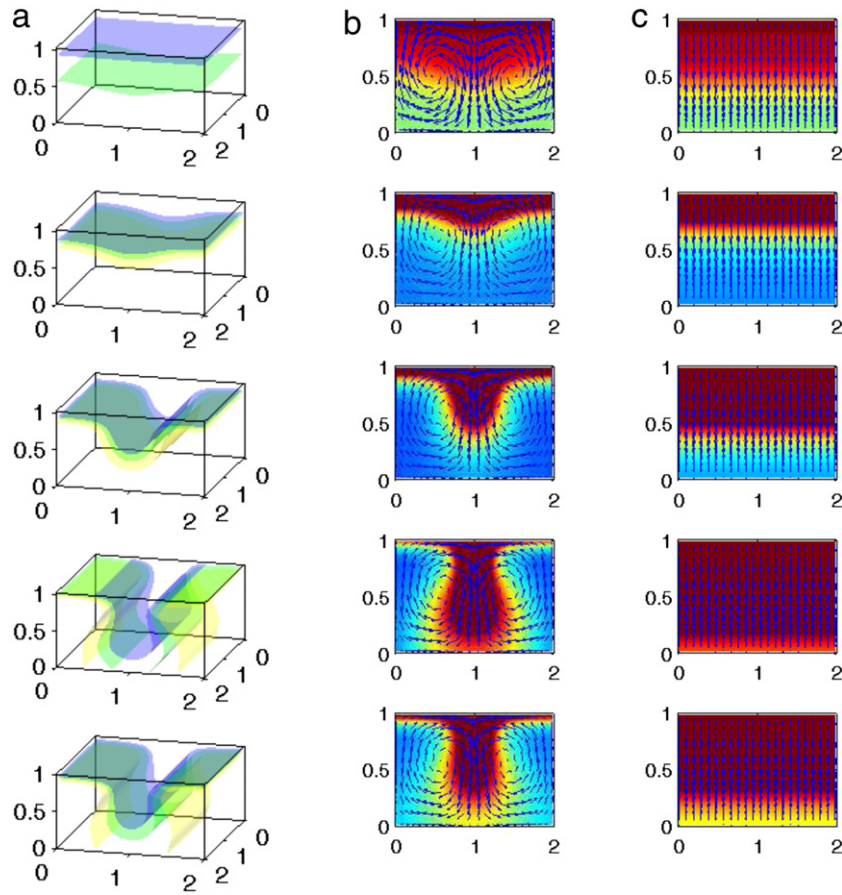
Fig. 14. For $n_{2D}^0(x, y, z)$, (a) cell density $n(x, y, z, t)$ and (b)–(c) bioconvection patterns in the x–z cross section at $y = 1$ and the y–z cross section at $x = 1$ at different times $t = 0.01, 0.2, 0.24, 0.29,$ and 0.59 (from top to bottom). In (a), yellow, green, and blue isosurfaces correspond to $n(x, y, z, t) = 0.5, 0.75,$ and 1, respectively. In (b) (or (c)), color contours represent the cell concentration $n(x, 1, z, t)$ (or $n(1, y, z, t)$) with red representing large concentrations and blue representing small concentrations, and arrows represent the velocity components $u(x, 1, z, t)$ and $w(x, 1, z, t)$ (or $v(1, y, z, t)$ and $w(1, y, z, t)$). (For interpretation of the references to color in this figure legend, the reader is referred to the web version of this article.)

$c^0(x, y, z) = 1,$ $\mathbf{u}^0(x, y, z) = \mathbf{0}$ on the domain

$\Omega = [0, 4] \times [0, 2] \times [0, 1]$

and with various values of δ : $\delta = 5, 25,$ and 50 with D_n fixed. The remaining parameters are $\alpha = 10, \beta = 10, \gamma = 1000,$ and $Sc = 500$.

Figs. 10–12 show the results with $\delta = 5, 25,$ and 50, respectively. In each figure, (a) and (b) show cell density $n(x, y, z, t)$ and bioconvection pattern in the x–z cross section at $y = 1$ at different times, respectively. For $\delta = 5$ (Fig. 10), the time evolution of the plumes is similar to the case of Fig. 9. However, for $\delta = 25$ and 50 (Figs. 11 and 12, respectively), the results are different significantly. The increased diffusive oxygen replenishment, caused if the case where D_c is increased is considered, results in reduced cell upswimming throughout the chamber and relatively more cells are situated in the lower regions of the chamber. We also observe that the two instabilities are approaching each other and merge into one instability. This is a fluid-dynamic effect (similar to the merging of Rayleigh–Bénard convection cells [31–34]) rather than a chemotaxis effect.

4.4.4. Comparison of 2D and 3D bioconvection

In order to compare 2D and 3D bioconvection, we take $c^0(x, y, z) = 1, \mathbf{u}^0(x, y, z) = \mathbf{0}$, and the following two initial conditions for the cell density:

$$n_{3D}^0(x, y, z) = \begin{cases} 1 & \text{if } z > 0.499 - 0.05(\sin((x - 0.5)\pi) \\ & \quad + \sin((y - 0.5)\pi)), \\ 0.5 & \text{otherwise} \end{cases}$$

and

$$n_{2D}^0(x, y, z) = \begin{cases} 1 & \text{if } z > 0.499 - 0.05 \sin((x - 0.5)\pi), \\ 0.5 & \text{otherwise} \end{cases}$$

on the domain $\Omega = [0, 2] \times [0, 2] \times [0, 1]$.

Figs. 13 and 14 show the results with $n_{3D}^0(x, y, z)$ and $n_{2D}^0(x, y, z)$, respectively. In each figure, (a), (b), and (c) show cell density $n(x, y, z, t)$ and bioconvection patterns in the x–z cross section at $y = 1$ and the y–z cross section at $x = 1$ at different times, respectively. In the case of 3D ($n_{3D}^0(x, y, z)$, Fig. 13), the cells move into the center of the plume in both x and y directions due to 3D bioconvection and, thus, the plume hits the bottom of the chamber more rapidly than the case of 2D ($n_{2D}^0(x, y, z)$, Fig. 14).

5. Conclusions

We investigated numerically the nonlinear dynamics of a three-dimensional chemotaxis–fluid system without linearization and axisymmetry. We used an operator splitting-type Navier–Stokes solver to avoid a too strong restriction on the time step due to a high Schmidt number. Through numerical examples, we observed the formation of falling plumes and the convergence towards numerically stable stationary plumes. And the merging of neighboring plumes was observed for a specific parameter set.

Acknowledgments

References

[1] A.J. Hillesdon, T.J. Pedley, J.O. Kessler, The development of concentration gradients in a suspension of chemotactic bacteria, Bull. Math. Biol. 57 (1995) 299–344.
[2] C. Dombrowski, L. Cisneros, S. Chatkaew, R.E. Goldstein, J.O. Kessler, Self-concentration and large-scale coherence in bacterial dynamics, Phys. Rev. Lett. 93 (2004) 098103.
[3] I. Tuval, L. Cisneros, C. Dombrowski, C.W. Wolgemuth, J.O. Kessler, R.E. Goldstein, Bacterial swimming and oxygen transport near contact lines, Proc. Natl. Acad. Sci. 102 (2005) 2277–2282.
[4] A.V. Kuznetsov, The onset of thermo-bioconvection in a shallow fluid saturated porous layer heated from below in a suspension of oxytactic microorganisms, Eur. J. Mech. B Fluids 25 (2006) 223–233.
[5] A.V. Kuznetsov, Non-oscillatory and oscillatory nanofluid bio-thermal convection in a horizontal layer of finite depth, Eur. J. Mech. B Fluids 30 (2011) 156–165.
[6] S. Ghorai, M.K. Panda, Bioconvection in an anisotropic scattering suspension of phototactic algae, Eur. J. Mech. B Fluids 41 (2013) 81–93.
[7] H. Xu, I. Pop, Fully developed mixed convection flow in a horizontal channel filled by a nanofluid containing both nanoparticles and gyrotactic microorganisms, Eur. J. Mech. B Fluids 46 (2014) 37–45.
[8] A.J. Hillesdon, T.J. Pedley, Bioconvection in suspensions of oxytactic bacteria: linear theory, J. Fluid Mech. 324 (1996) 223–259.
[9] A.M. Metcalfe, T.J. Pedley, Bacterial bioconvection: weakly nonlinear theory for pattern selection, J. Fluid Mech. 370 (1998) 249–270.
[10] A. Lorz, Coupled chemotaxis fluid model, Math. Models Methods Appl. Sci. 20 (2010) 987–1004.
[11] R. Duan, A. Lorz, P. Markowich, Global solutions to the coupled chemotaxis-fluid equations, Comm. Partial Differential Equations 35 (2010) 1635–1673.
[12] M. di Francesco, A. Lorz, P. Markowich, Chemotaxis-fluid coupled model for swimming bacteria with nonlinear diffusion: global existence and asymptotic behavior, Discrete Contin. Dyn. A 28 (2010) 1437–1453.
[13] A. Harashima, M. Watanabe, I. Fujishiro, Evolution of bioconvection patterns in a culture of motile flagellates, Phys. Fluids 31 (1988) 764–775.
[14] S. Ghorai, N.A. Hill, Development and stability of gyrotactic plumes in bioconvection, J. Fluid Mech. 400 (1999) 1–31.
[15] S. Ghorai, N.A. Hill, Periodic arrays of gyrotactic plumes in bioconvection, Phys. Fluids 12 (2000) 5–22.
[16] S. Ghorai, N.A. Hill, Wavelengths of gyrotactic plumes in bioconvection, Bull. Math. Biol. 62 (2000) 429–450.
[17] S. Ghorai, N.A. Hill, Axisymmetric bioconvection in a cylinder, J. Theoret. Biol. 219 (2002) 137–152.
[18] A. Chertock, K. Fellner, A. Kurganov, A. Lorz, P.A. Markowich, Sinking, merging and stationary plumes in a coupled chemotaxis-fluid model: a high-resolution numerical approach, J. Fluid Mech. 694 (2012) 155–190.
[19] M.M. Hopkins, L.J. Fauci, A computational model of the collective fluid dynamics of motile micro-organisms, J. Fluid Mech. 455 (2002) 149–174.
[20] S. Ghorai, N.A. Hill, Gyrotactic bioconvection in three dimensions, Phys. Fluids 19 (2007) 054107.
[21] A. Karimi, M.R. Paul, Bioconvection in spatially extended domains, Phys. Rev. E 87 (2013) 053016.
[22] F.H. Harlow, J.E. Welch, Numerical calculation of time-dependent viscous incompressible flow of fluid with free surface, Phys. Fluids 8 (1965) 2182–2189.
[23] J. Stam, Stable fluids, in: W. Waggenspack (Ed.), Proceedings of the 26th Annual Conference on Computer Graphics and Interactive Techniques, ACM Press, New York, 1999, pp. 121–128.
[24] A.J. Chorin, A numerical method for solving incompressible viscous flow problems, J. Comput. Phys. 2 (1967) 12–26.
[25] U. Trottenberg, C. Oosterlee, A. Schüller, Multigrid, Academic Press, London, 2001.
[26] H.C. Ku, R.S. Hirsh, T.D. Taylor, A pseudospectral method for solution of the three-dimensional incompressible Navier–Stokes equations, J. Comput. Phys. 70 (1987) 439–462.
[27] B.N. Jiang, T.L. Lin, L.A. Povinelli, Large-scale computation of incompressible viscous flow by least-squares finite element method, Comput. Methods Appl. Mech. Engrg. 114 (1994) 213–231.
[28] D.C. Lo, K. Murugesan, D.L. Young, Numerical solution of three-dimensional velocity–vorticity Navier–Stokes equations by finite difference method, Internat. J. Numer. Methods Fluids 47 (2005) 1469–1487.
[29] H. Ding, C. Shu, K.S. Yeo, D. Xu, Numerical computation of three-dimensional incompressible viscous flows in the primitive variable form by local multiquadric differential quadrature method, Comput. Methods Appl. Mech. Engrg. 195 (2006) 516–533.
[30] J.T. Holdeman, A velocity-stream function method for three-dimensional incompressible fluid flow, Comput. Methods Appl. Mech. Engrg. 209–212 (2012) 66–73.
[31] C.J. Chapman, M.R.E. Proctor, Nonlinear Rayleigh–Bénard convection between poorly conducting boundaries, J. Fluid Mech. 101 (1980) 759–782.
[32] F.H. Busse, Transition to turbulence in Rayleigh–Bénard convection, in: Hydro-dynamic Instabilities and the Transition to Turbulence, Springer, Berlin, 1985, pp. 97–137.
[33] F.H. Busse, M. Sieber, Regular and chaotic patterns of Rayleigh–Bénard convection, in: Bifurcation and Chaos: Analysis, Algorithms, Applications, Birkhäuser, Basel, 1991, pp. 79–92.
[34] A. Bayliss, T.-K. Ma, B.J. Matkowsky, C.W. Wahle, The reactive Rayleigh–Bénard problem with throughflow, SIAM J. Appl. Math. 61 (2000) 1103–1142.